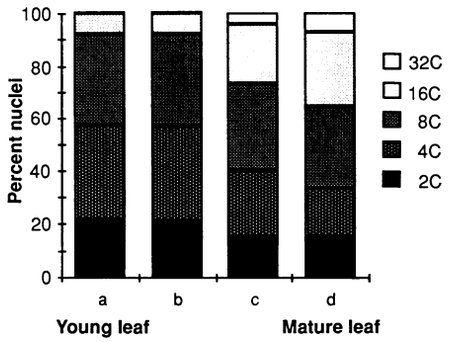

Fig. 2. The change in ploidy distribution with leaf development. Average ploidy distributions for four sets of leaves from three plants are shown starting with (a) the topmost leaf pair through the (b) second, (c) third, and (d) fourth leaf pair down the central axis of the plant. Standard errors range from 0.6 to 6.0.

fully expanded mature leaf is primarily the result of cell expansion. The higher proportion of low ploidy nuclei in young leaves may result from the developmental program. The high rate of cell division in early leaf development may delay the accumulation of cells with elevated genome copy numbers.

When *M. crystallinum* is subjected to high NaCl or drought stress, it undergoes a major physiological and metabolic conversion from C_3 to CAM (crassulacean acid metabolism) CO_2 fixation (*9*) as a result of altered gene expression (*10*). This conversion is a water conservation strategy. Because differences in gene copy number could be one aspect of changes in gene expression in response to stress, ploidy distributions were determined for nuclei from leaves and roots of nonstressed and NaCl-stressed plants (*11*). No significant differences in ploidy distribution in response to salt stress were observed in five independent experiments. Subtle changes that might be limited to a specific cell type within these tissues are not ruled out.

Multiploidy was not observed in 39 plant species previously analyzed by slow cytometry (*12*). Since *M. crystallinum* differs from these other plants in that it is a succulent CAM plant, we analyzed nuclei from the leaves of ten other succulent CAM species to test the possibility that multiploidy is associated with succulence or CAM. We have identified eight species that exhibit multiple ploidy at least in their leaves and two species that do not (Table 1). As does *M. crystallinum*, the eight multiple ploidy species have a small genome size, and 2C nuclei make up only a minor part of the total nuclei population. Two species of aloe, although succulent CAM plants, do not exhibit multiple classes of ploidy. These aloes are distinct from the other succulents in that they have very large genomes. This agrees with the observation that the tendency for somatic polyploidization in plants is inversely related to genome size and that somatic polyploidization in small genome plants and germline polyploidization in large genome plants may be two strategies for accomplishing a similar result (*13*). Multiple ploidy is not exhibited by 16 nonsucculent species that have genome sizes similar to the multiploid succulents (Table 2). Multiploidy may be a general property of succulents that have small genomes. The function of multiploidy in these plants is unknown. In mature *M. crystallinum* leaves, the presence of a range of ploidy, including 2C, indicates that not all cells are destined to become endopolyploid. The gradual shift in the bias of ploidy distributions toward higher levels seen during leaf development stops once the leaf is fully expanded. A ploidy distribution is then maintained that is typical of mature leaves. This pattern of differential endopolyploidization may be linked to the process of cellular differentiation that yields the different types of cells present in the mature leaf. Cells that could reasonably be expected to reach high levels of ploidy are large-volume cells such as the water-storing mesophyll cells that give the leaves the property of succulence. The capacity for synthesis from a small genome may be insufficient for the large volume of these cells. For succulents, it may be that large genomes and multiploidization of small genomes are alternative strategies for adaptation to arid environments. Correlation of ploidy with particular cell types would give clues as to the possible role of multiploidy in these plants.

REFERENCES AND NOTES

1. W. Nagl, *Annu. Rev. Plant Physiol.* **27**, 39 (1976).
2. M. D. Bennett and J. D. Smith, *Proc. R. Soc. London Ser. B* **274**, 227 (1976).
3. Y. K. Bansal and S. Sen, *Nucleus* (Calcutta) **28**, 183 (1985).
4. W. Nagl, *Z. Pflanzenphysiol.* **73**, 1 (1974); S. S. Dhillon and J. P. Miksche, *Am. J. Bot.* **69**, 219 (1982); M. F. Le Gal, F. M. Lecocq, J. N. Hallet, *Protoplasma* **130**, 128 (1986).
5. F. D'Amato, *CRC Crit. Rev. Plant Sci.* **3**, 73 (1986).
6. D. W. Galbraith *et al.*, *Science* **220**, 1049 (1983).
7. The DNA contents (picograms) and standard errors (n = 6) for 2C, 4C, 8C, 16C, and 32C nuclei were, respectively, 0.86 ± 0.034, 1.77 ± 0.047, 3.47 ± 0.087, 6.72 ± 0.216, and 13.06 ± 0.893.
8. L. S. Leutwiler, B. R. Hough-Evans, E. M. Meyerowitz, *Mol. Gen. Genet.* **194**, 15 (1984).
9. K. Winter and D. J. von Willert, *Z. Pflanzenphysiol.* **67**, 166 (1972).
10. J. C. Cushman, G. Meyer, C. B. Michalowski, J. M. Schmitt, H. J. Bohnert, *Plant Cell.* **1**, 715 (1989).
11. Data not shown. Plants (*M. crystallinum*) were salt-stressed by the addition of NaCl to nutrient solution in a concentration of 500 mM. Plants were stressed 5, 10, and 28 days.
12. K. Harkins, personal communication.
13. W. Nagl, *Nature* **261**, 614 (1976).
14. V. H. Heywood, Ed., *Flowering Plants of the World* (Mayflower Books, New York, 1978).

15. We thank J. Van't Hof, V. Walbot, and J. Cushman for critical reading of the manuscript, and B & B Cactus Farm of Tucson, Arizona, for supplying several species of succulents. Supported by Arizona Agricultural Experimental Station (174452) and USDA-CRGP-89-37264-4711 (E.J.D. and H.J.B.) and by NSF DIR-8709697 (K.R.H. and D.W.G.). Cell sorter purchased by Agricultural Research Laboratory Biotechnology Program and DOE DE-FG05-88ER75457.

28 February 1990; accepted 11 July 1990

Photoacoustic "Signatures" of Particulate Matter: Optical Production of Acoustic Monopole Radiation

G. J. DIEBOLD, M. I. KHAN, S. M. PARK*

Absorption of pulsed laser radiation by a single particle generates a photoacoustic wave whose time profile can be measured with a wideband pressure transducer. Solution of the wave equation for pressure in one, two, and three dimensions shows that the photoacoustic wave is determined by the geometry and dimensions of the particle, and by its sound speed and density relative to the fluid that surrounds it. Photoacoustic waves, referred to here as signatures, are reported in experiments in which fluid droplets, cylinders, and layers are irradiated with 10-nanosecond laser pulses.

THE ABSORPTION OF OPTICAL RADIATION by matter causes heating and, in general, subsequent expansion of the irradiated body, thereby launching an acoustic wave. Owing to its high sensitivity and its response to evolved heat, this process, known as the photoacoustic effect, has found application in a number of fields including spectroscopy, nondestructive testing, photochemistry, microscopy, semiconductor physics, and trace detection (*1*). We report here a study of a facet of the photoacoustic effect that has heretofore received only scant attention: the temporal profile of acoustic waves generated by particulate mat-

Department of Chemistry, Brown University, Providence, RI 02912.

*Present address: Department of Chemistry, University of Illinois at Chicago, Chicago, IL 60680.

ter (*2, 3*). The results given here for spheres, cylinders, and slabs show the photoacoustic waveforms to be rich in detail as determined by the acoustic and geometric properties of the irradiated particle.

Consider a spherical fluid droplet irradiated by sinusoidally modulated radiation. The acoustic pressure p can be found as a solution to the wave equation for pressure (*3, 4*)

$$\left(\nabla^2 - \frac{1}{c^2}\frac{\partial^2}{\partial t^2}\right)p = -\frac{\beta}{C_p}\frac{\partial H}{\partial t} \quad (1)$$

where c is the sound speed, t is the time, β is the volume expansion coefficient, C_p is the heat capacity, and H is the heat deposited per unit volume and time in the particle. If the droplet is optically thin, the pressure from the optical deposition of energy is uniform throughout the droplet, and Eq. 1 can be integrated immediately to give a source term. The total acoustic pressure inside the sphere is described by the source term plus a solution to the homogeneous wave equation; the pressure outside the sphere is described by a spherical wave propagating radially outward from the droplet. Imposition of the acoustic conservation laws (*4*) for pressure and acceleration at the interface between the sphere and the surrounding fluid then gives an expression for the pressure as a function of modulation frequency.

The most common experimental technique, however, uses pulsed radiation to generate an acoustic signal that is recorded in time. The corresponding theoretical expression is easily obtained from the frequency domain result by simple Fourier transformation, which gives the photoacoustic signal for short pulse excitation (*5*) as

$$p(t) = \frac{i\kappa}{2\pi\hat{r}}\int_{-\infty}^{\infty} \frac{(\sin q - q\cos q)\, e^{-iq\hat{\tau}}}{q^2[(1-\hat{\rho})(\sin q/q) - \cos q + i\hat{\rho}\hat{c}\sin q]}dq \quad (2)$$

where $\kappa = \alpha\beta E_0 c_s^2/C_p$, E_0 is the energy per unit area in the exciting light beam, α is the optial absorption coefficient, c_s is the sound speed in the droplet, $\hat{r}$ is the distance from the droplet divided by the radius of the droplet a, $\hat{\rho}$ is the density of the droplet divided by the density of the surrounding fluid, $\hat{c}$ is the sound speed in the droplet divided by that in the surrounding fluid, and $\hat{\tau}$ is the dimensionless retarded time (*6*) from the surface of the droplet.

Physically, the rapid deposition of heat by absorption of optical radiation causes an immediate and uniform increase in the pressure of the droplet. The release of this pressure in time through expansion of the droplet against the surrounding fluid gives rise to an ultrasonic wave whose temporal characteristics, according to Eq. 2, depend on only three parameters: the density ratio $\hat{\rho}$, the sound speed ratio $\hat{c}$, and the retarded time $\hat{\tau}$ [which is a function of the radius and sound speed of the droplet (*6*)]. A second point regarding Eq. 2 is that the integral can be evaluated quickly and conveniently on a digital computer by means of the fast Fourier transform algorithm.

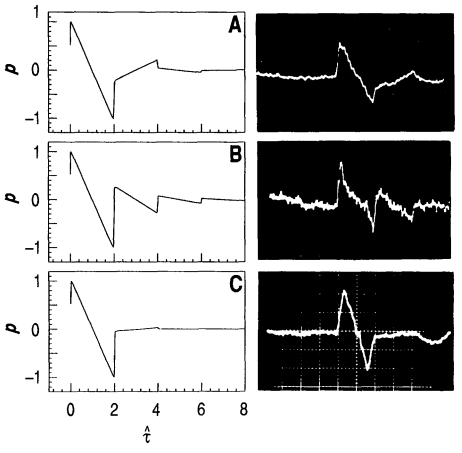

Fig. 1. Calculated pressure p (in arbitrary units) versus dimensionless time $\hat{\tau}$ from Eq. 2 for fluid droplets with $\hat{\rho} = 1$. (**A**) Hexane–carbon tetrachloride (CCl_4) droplet suspended in water ($\hat{\rho} = 1.01$, $\hat{c} = 0.645$, $a = 0.5$ mm). (**B**) Formamide droplet suspended in a hexane-CCl_4 mixture ($\hat{\rho} = 1.00$, $\hat{c} = 1.65$ $a = 1.5$ mm). (**C**) 1,2,3,4-Tetrahydronaphthalene (tetralin) droplet in water ($\hat{\rho} = 0.97$, $\hat{c} = 0.962$, $a = 1.4$ mm). The experimental time scales are 500 ns per division in the top oscillogram and 1 μs per division in the other two. The slight departure of the formamide wave form from the predicted shape is caused by the addition of extra dye, which was necessitated by the small expansion coefficient of formamide and the consequent low signal-to-noise ratio in the recorded wave.

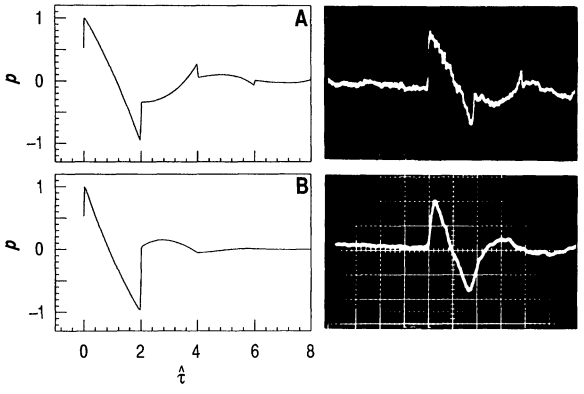

Fig. 2. Photoacoustic wave forms for droplets where $\hat{\rho} \neq 1$. (**A**) Hexane droplet in water ($\hat{\rho} = 0.66$, $\hat{c} = 0.708$, $a = 1$ mm). (**B**) CCl_4 droplet in water ($\hat{\rho} = 1.6$, $\hat{c} = 0.618$, $a = 1$ mm). The time scale in both oscillograms is 1 μs per division.

To test the validity of Eq. 2, we used the 532-nm harmonic of a pulsed Nd:YAG (yttrium-aluminum-garnet) laser as a radiation source (*7*). The laser output is directed through an aperture onto a droplet located in a photoacoustic cell. The droplet, which contains a small amount of dye, is suspended at the end of a fine capillary. The droplet and the transparent fluid that fills the cell are of differing polarities so that the dye remains dissolved only in the droplet. The photoacoustic cell is equipped with a wideband polyvinylidiene fluoride transducer (*8*), 50 μm thick and 3 mm in diameter. The output of the transducer is fed to a fast, high-input impedance preamplifier (Comlinear Inc., model E103-1M), whose output is displayed on an oscilloscope. A laser fluence of about 10 to 100 J/m^2 gives an adequate signal-to-noise ratio for direct recording of the wave forms in most experiments.

The first experiments were done with droplets whose densities were adjusted to match those of the surrounding fluids. Under the condition $\hat{\rho} = 1$, Eq. 2 can be evaluated in closed form to give

$$p(t) = \frac{\kappa}{(1+\hat{c})\hat{r}}\sum_{n=0}^{\infty}(2n + 1 - \hat{\tau})(-\xi)^n\tilde{\Theta}_{2n,2n+2}(\hat{\tau}) \quad (3)$$

where $\xi = (1-\hat{c})/(1+\hat{c})$ and $\tilde{\Theta}_{i,j}(\hat{\tau})$ is a square wave function that is unity for values of $\hat{\tau}$ between i and j and is zero otherwise. The photoacoustic wave described by Eq. 3 is a series of N-shaped waves whose amplitudes decrease in time according to the magnitude of ξ. For $\hat{c}$ greater than one, each of the waves is in phase; for $\hat{c}$ less than one, each wave described by an odd value of n is inverted. Numerically calculated and experimental wave forms for droplets with $\hat{\rho}$ approximately equal to one are given in Fig. 1. The alternating sign of the amplitude of successive N waves for positive values of ξ (that is, for $\hat{c} < 1$) is clearly evident in Fig. 1A. A single N wave can be seen when the parameter ξ equals zero, as is approximated in Fig. 1C. The same N wave is produced by a bursting balloon (*4*), a classic acoustics problem analogous to the photoacoustic effect discussed here.

When the density ratio differs from one, in general, Eq. 2 must be evaluated numerically to obtain the acoustic wave form. Examples where $\hat{\rho}$ is less than and greater

than one are shown in Fig. 2. In the latter case it can be shown (*5*) that the wave is a decreasing exponential for $0 < \hat{\tau} < 2$.

Wave forms for the photoacoustic effect generated by short-pulse irradiation of an infinite cylinder are found as described above for a sphere, except that the solutions of the wave equation are *n*th order Bessel functions J_n and Hankel functions H_n. The photoacoustic signal again is found in integral form as

$$p(t) = \frac{i\kappa}{2\pi}\int_{-\infty}^{\infty} \frac{J_1(q)H_0(\hat{r}q)e^{iq\hat{t}}}{q[J_1(q)H_0(\hat{c}q) - \hat{\rho}\hat{c}J_0(q)H_1(\hat{c}q)]}\,dq \quad (4)$$

where $\hat{t}$ is the (dimensionless) time after firing of the laser (*6*) and $\hat{r}$ is the distance from the cylinder divided by the radius of the cylinder, *a*.

Fluid cylinders are produced by the pumping of organic solvents (immiscible with water) through narrow-bore liquid chromatography tubing into a water-filled photoacoustic cell. By judicious adjustment of the flow rate of the pump, a narrow cylindrical stream of flowing solvent about 1 cm long is formed. (The stream eventually breaks up to form droplets.) Irradiation of a section of the cylinder that is long compared with its radius approximates the response of an infinite cylinder. Photoacoustic wave forms obtained by numerical evaluation of Eq. 4 and by irradiation of dyed cylinders with pulsed laser radiation are shown in Fig. 3. An obvious feature of the wave forms in Fig. 3A that distinguishes them from those generated by spheres is the slow approach of the pressure to the baseline at long times. This feature is a general characteristic of waves in two dimensions, as has been noted previously (*9*). Unlike the simple *N*-shaped wave form obtained for the sphere, the wave form generated by the cylinder for the case of identical densities and sound speeds $\hat{\rho} = \hat{c} = 1$ is a complicated function of time described by a hypergeometric function. However, the repetition of the initial wave form in time, seen in the wave forms generated by the sphere for $\hat{\rho} \neq 1$ and $\hat{c} \neq 1$, is clearly evident in the wave forms shown in Fig. 3, B and C.

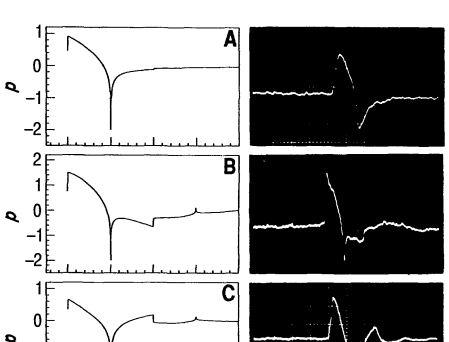

Fig. 3. Calculated (Eq. 4) and experimental photoacoustic wave forms for cylinders in water. (**A**) Tetralin cylinder in water ($\hat{\rho} = 0.97$, $\hat{c} = 0.960$, $a = 0.2$ mm). (**B**) Hexane cylinder in water ($\hat{\rho} = 0.66$, $\hat{c} = 0.708$, $a = 0.25$ mm. (**C**) Bromoform cylinder in water ($\hat{\rho} = 2.9$, $\hat{c} = 0.61$, $a = 0.3$ mm). The time scales in the oscillograms are 200 ns per division in the top trace and 500 ns per division in the other two.

Photoacoustic wave forms generated by short-pulse irradiation of an infinite layer of absorbing fluid surrounded by a transparent fluid on both sides are found as described above for a sphere except that plane waves are taken as solutions to the wave equation. The acoustic pressure for the wave traveling along the positive *z* axis is again given as a Fourier integral,

$$p(t) = \frac{i\kappa}{2\pi}\int_{-\infty}^{\infty} \frac{\sin q e^{-iq\hat{\tau}}}{q(\sin q + i\hat{\rho}\hat{c}\cos q)}\,dq \quad (5)$$

where $\hat{\tau}$ is the retarded time from the edge of the layer. In contrast to the expressions obtained for the sphere and the cylinder, in Eq. 5 the parameters $\hat{\rho}$ and $\hat{c}$ appear only as a product and hence are not independent quantities in their influence on the acoustic wave. The denominator in Eq. 5 can be expanded in exponential functions and integrated to give the acoustic pressure as

$$p(t) = \frac{\kappa}{(1 + \hat{\rho}\hat{c})}\sum_{n=0}^{\infty} \zeta^n \tilde{\Theta}_{2n,2n+2}(\hat{\tau}) \quad (6)$$

where $\zeta = (1 - \hat{\rho}\hat{c})/(1 + \hat{\rho}\hat{c})$. This solution is analogous to Eq. 3 given for the sphere except that the expansion describes a series of square waves as opposed to *N*-shaped waves in time. Depending on the sign of ζ, alternating compressions and rarefactions in the photoacoustic wave are produced in analogy with the alternating sign of the *N* waves generated by the sphere when $\hat{\rho} = 1$. In order to do experiments with fluid layers, the 532-nm laser beam was expanded to cover an area of an absorbing fluid layer whose lateral dimensions were large compared with the thickness of the layer. The wave forms in Fig. 4 correspond to cases where $\zeta = 0$, $\zeta > 1$, and $\zeta < 1$.

In addition to the features of the wave forms discussed above, the solutions to the acoustic wave equation given by Eqs. 2, 4, and 5 are rich in their description of a variety of mechanical motions of fluid bodies. For example, the frequency domain analogs of these three equations show the effects of constructive and destructive interference, and radiative damping in the acoustic amplitude at an observation point. At high values of the density ratio, the radial and longitudinal eigenfrequencies for the three bodies discussed here are clearly identified as peaks in a plot of photoacoustic amplitude versus modulation frequency.

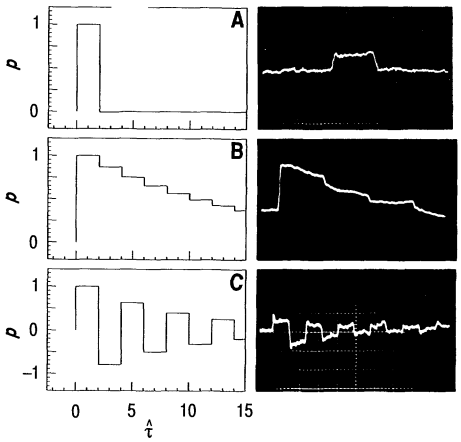

Fig. 4. Calculated (Eq. 5) and experimental photoacoustic wave forms for fluid layers (*11*). (**A**) A 2-mm-thick water layer floating between CCl_4 and castor oil ($\hat{\rho}\hat{c} = 1.03$). (**B**) A 1.5-mm acetone layer surrounded by Pyrex glass ($\hat{\rho}\hat{c} = 0.074$). (**C**) A 2.5-mm-thick colored glass slab in water ($\hat{\rho}\hat{c} = 9.4$). The time scales are 500 ns per division in each trace.

For the sphere, in particular, evaluation of Eq. 3 at low density gives a damped, low-frequency wave whose angular frequency of oscillation is given by $(c_s/a)(3\hat{\rho})^{1/2}$. Physically, the low-density limit corresponds to a rapidly heated gas bubble oscillating in a dense fluid. The oscillation frequency found here is in agreement with a previous calculation for a gas bubble (*10*). For light pulses whose duration is long (compared with the acoustic transit time across the sphere), the droplet generates a photoacoustic wave proportional to the first derivative of the radiation intensity; the fluid layer, on the other hand, generates a wave linearly proportional to the light intensity. Photoacoustic signatures that reflect the particle's geometry and dimensions and the acoustic parameters $\hat{\rho}$ and $\hat{c}$ are produced only when the duration of the light pulse is short compared with the sonic transit time across the particle.

The word "particle" is used broadly here, since solutions for the photoacoustic effect generated by isotropic solids have been obtained as well; the fluid body solutions are a special case of the solutions for solid bodies where the transverse sound speed is set to zero. The theoretical expressions predict wave forms with somewhat more complicated time dependences than those found for fluids, but again with features characteristic of the geometrical and acoustic properties of the irradiated body. Further experiments with bodies whose dimensions are smaller than those reported here are in progress.

The wave equation for pressure given above has a direct analog in electromagnetic theory, where the scalar potential (for the electric field) replaces the pressure, and the charge density constitutes the source rather than the heat deposition rate. Given this simple analogy and the comprehensive investigation of Maxwell's equations that has taken place over the last century, it is natural to ask why electromagnetic solutions analogous to Eqs. 2, 4, and 5 have not appeared. The answer to this question lies in an important distinction between the kinds of sources that are possible according to acoustic and electromagnetic theory: the photoacoustic wave forms described here arise from monopole radiation resulting from a uniform expansion of the body that is naturally produced by the absorption of radiation—the analogous rapid switching on of a macroscopic quantity of electrical charge of a single polarity that would constitute a monopole source of electromagnetic radiation is not possible under the restriction of charge conservation.

REFERENCES AND NOTES

1. P. Hess, Ed. *Photoacoustic, Photothermal and Photochemical Processes in Gasses* (Springer-Verlag, Heidelberg, 1989); M. W. Sigrist, *J. Appl. Phys.* **60**, R83 (1986); A. C. Tam, *Rev. Mod. Phys.* **58**, 381 (1986); E. Luscher, H. J. Coufal, P. Korpium, R. Tilgner, Eds., *Photoacoustic Effect, Principles and Applications*, (Viewig, Braunschweig, West Germany, 1984); A. C. Tam, in *Ultrasensitive Laser Spectroscopy*, D. S. Kilger, Ed. (Academic Press, New York, 1983), pp. 1–108.
2. The photoacoustic effect in a homogeneous medium has been discussed by a number of investigators, including: H. C. Hu, *J. Acoust. Soc. Am.* **48**, 2245 (1969); J. M. Heritier, *Opt. Commun.* **44**, 267 (1983); H. M. Lai and K. Young, *J. Acoust. Soc. Am.* **72**, 2000 (1982); L. M. Lyamshev, *Sov. Phys. Usp.* **24**, 977 (1981); L. M. Lyamshev and L. V. Sedov, *Sov. Phys. Acoust.* **27**, 4 (1981); N. W. Sigrist and F. K. Kneubuhl, *J. Acoust. Soc. Am.* **64**, 1652 (1978). Some work has been published where acoustic waves are generated by thermal conduction. See A. Yoshinaga, Y. Hsieh, T. Sawada, Y. Gohshi, *Anal. Sci.* **5**, 147 (1989); T. Kitamori and M. Fujii, *J. Appl. Phys.* **58**, 1456 (1985); C. W. Bruce and R. G. Pinnick, *Appl. Opt.* **16**, 1762 (1977); Z. Yasa, N. Amer, H. Rosen, A. D. Hansen, T. Novakov, *ibid.* **18**, 2428 (1979).
3. The wave equation for pressure can be used when heat conduction can be neglected on the time scale for sound wave generation.
4. P. J. Westervelt and R. S. Larson, *J. Acoust. Soc. Am.* **54**, 121 (1973); S. Temkin, *Elements of Acoustics* (Wiley, New York, 1981).
5. G. J. Diebold and P. J. Westervelt, *J. Acoust. Soc. Am.* **84**, 2245 (1988).
6. Specifically, the retarded time is defined as $\hat{\tau} = (c_s/a)[t - (r - a)/c_f]$ for a sphere, where t is the time after firing of the laser, a is the radius of the sphere, and c_f is the sound speed in the fluid. For a cylinder $\hat{\tau}$ and κ are given by the same expression, but $\hat{r}$ is expressed in polar coordinates, c_s refers to the sound speed in the cylinder, a is the radius of the cylinder, and $t = c_s t/a$. For a fluid layer, $\hat{\tau} = (2c_f/a)[t - (z - a/2)/c_f]$, where a now refers to the thickness of the layer and c_f is the sound speed in the slab. The parameter κ in these three geometries refers to quantities in the radiation-absorbing medium.
7. The rise times and other high-frequency features of the experimental wave forms are intrinsically limited by the finite duration of the laser pulse (approximately 10 ns here), and by viscous effects in the fluid that have not been taken into account in the theory. In the case of spherical and cylindrical waves, integration of the wave forms over the face of the detector also causes an apparent decrease in the recorded rise time. These effects are clearly evident in the cylindrical wave forms. The dimensions of the spheres and cylinders are determined by measuring the shadows they cast on a screen. For features δ of the wave forms that correspond to transit times across the particles, agreement with theory to within 20% is obtained in all the experiments.
8. H. Coufal, in *Photoacoustic and Photothermal Phenomena*, P. Hess and J. Pelzl, Eds. (Springer-Verlag, Heidelberg, 1988), pp. 464–469.
9. L. D. Landau and E. M. Lifshitz, *Fluid Mechanics* (Pergamon, New York, 1987), p. 273.
10. R. B. Lindsay, *Mechanical Radiation* (McGraw-Hill, New York, 1960).
11. Glass supports a shear wave and cannot be considered as a fluid. However, for a plane wave directed at perpendicular incidence to an infinite solid surface, no transverse wave is generated and the analysis given here remains valid.

12. We are grateful to P. J. Westervelt for his helpful contributions and discussion and to J. Taylor and R. Boyles for their skillful construction of the experimental apparatus. Supported under grant ER13235 from the U.S. Department of Energy Office of Basic Energy Sciences.

10 April 1990; accepted 29 June 1990

A Bangiophyte Red Alga from the Proterozoic of Arctic Canada

NICHOLAS J. BUTTERFIELD, ANDREW H. KNOLL, KEENE SWETT

Silicified peritidal carbonate rocks of the 1250- to 750-million-year-old Hunting Formation, Somerset Island, arctic Canada, contain fossils of well-preserved bangiophyte red algae. Morphological details, especially the presence of multiseriate filaments composed of radially arranged wedge-shaped cells derived by longitudinal divisions from disc-shaped cells in uniseriate filaments, indicate that the fossils are related to extant species in the genus *Bangia*. Such taxonomic resolution distinguishes these fossils from other pre-Edicaran eukaryotes and contributes to growing evidence that multicellular algae diversified well before the Ediacaran radiation of large animals.

MULTICELLULAR ORGANISMS characterized by cellular integration and differentiation occur in all four eukaryotic kingdoms, including at least eight separate phyla in the Protista (*1*). Most of these experiments in complex multicellularity must have made their first appearance well before the Edicaran radiation of large animals (600 million years ago, Ma), but fossil evidence is limited and in many cases equivocal. Interpretational problems result from the lack of preserved cellular structure in many fossils, the nondiagnostic nature of such structures as may be preserved, and the absence of biochemical and ultrastructural information. In this report, we describe well-preserved fossils in 1250- to 750-million-year-old rocks from arctic Canada in which the habit and patterns of cell division are sufficiently distinctive to permit their assignment to the bangiophyte red algae.

The fossiliferous rocks were collected on Somerset Island, a narrowly separated extension of the Boothia Peninsula in the southeastern part of the Canadian arctic archipelago (District of Franklin, Northwest Territories) (Fig. 1). In the Aston Bay area on its northwest coast, little altered middle to upper Proterozoic sedimentary rocks sit on crystalline basement of the Canadian Shield (*2*). The sedimentary sequence comprises two unconformity-bounded units. The lower unit, the Aston Formation, consists largely of quartz arenite, whereas the overlying Hunting Formation is dominated by intertidal to supratidal carbonate rocks. The fossiliferous horizons are thin (1 cm thick) chert layers in stratiform laminated shallow-subtidal to intertidal carbonate rocks of the Hunting Formation, approximately 150 m above the Aston-Hunting contact.

Hunting deposition is only broadly constrained in time, bracketed by two generations of mafic dikes (*2*) that are dated elsewhere at 1267 ± 2 Ma (*3*) and 723 ± 3 Ma (*4*). Constituent stromatolites (stratiform to simple *Baicalia*-type columns) and associated microfossils (dense filamentous mats, spheroids, and the stalk-forming cyanobacterium *Polybessurus*) are useful as paleoenvironmental indicators but cannot provide finer time resolution. On the other hand, several analyses of Hunting carbonate rocks indicate that they have $\delta^{13}C$ values between +2.5 and +3.8 per mil (*5*), values lighter than those typical of 700- to 800-million-year-old carbonate rocks in the Canadian arctic and elsewhere (*5, 6*). The Hunting isotopic signature more closely approximates that of unweathered dolomite from the 1100- to

N. J. Butterfield and A. H. Knoll, Botanical Museum, Harvard University, Cambridge, MA 02138.
K. Swett, Department of Geology, University of Iowa, Iowa City, IA 52242.